

Monitoring Polysulfide Solubility and Diffusion in Fluorinated Ether-Based Electrolytes by Operando Raman Spectroscopy

Roza Bouchal^{†, [a]} Athmane Boulaoued^{†, [a]} and Patrik Johansson^{*[a, b]}

Polysulfide (PS) solubility is a key property of Li–S battery electrolytes for the conversion reaction(s) at the electrolyte–electrode interface. When PSs shuttle between the composite C/S cathode and the lithium metal anode, however, this leads to a continuous loss of active material and thus rapid capacity fading. In order to restrict the shuttle effect, fluorinated ethers have recently been proposed as a remedy; by only sparsely dissolving PSs they physically block the diffusion. We show here how the diffusion of PSs in fluorinated ethers, as monitored by operando Raman spectroscopy, is selective and that only short-chain PS (S_4^{2-}) are soluble and diffuse. This fundamental observation can be used to further leverage the practical performance of Li–S batteries by novel electrolyte design.

For a more sustainable future without fossil energy, the electrification of vital markets such as transportation and large-scale grid storage is a key, but they require high energy density batteries for longer driving ranges and smarter storage capabilities.^[1–3] Although current lithium-ion battery cells can reach up to *ca.* 300 W·h·kg⁻¹ these can hardly satisfy the fast-expanding demand,^[4] why the development of batteries with even higher energy density, longer cycle-life and acceptable levels of safety is critically needed.^[3,5,6] Lithium-sulfur (Li–S) batteries are considered as one of the most promising rechargeable battery technologies due to that sulfur is abundant and non-toxic, and meets the requirements of renewable and clean energy development.^[5,6] Today, Li–S battery cells can deliver 400–500 W·h·kg⁻¹, but only with a relatively short cycle-life, which considerably restricts any large-scale commercialization.^[7] The electrochemical reactions of Li–S

batteries involve complicated conversion reactions based on multi-electron transfer, generating a series of intermediate soluble polysulfide (PS) species Li_2S_n ($4 \leq n \leq 8$).^[8] The PS intermediates not only dissolve into the electrolyte, causing severe loss of active material, but also shuttle between the anode and the cathode without performing useful work. This shuttling results in low Coulombic efficiency, relatively short cycle-life, and increased internal cell resistance.^[9,10] Therefore, the control of PS solubility and diffusion are keys to achieve more performant Li–S batteries.

Several approaches have been used to tackle the shuttling,^[9] mainly by protecting the lithium surface by *e.g.* adding LiNO₃ to the electrolyte,^[11–14] but this is at the expense of reduced cell voltage and is seriously plagued by gradual decay upon cycling. Another approach is to trap the PS in or close to the C/S composite cathode.^[9,15] Yet, another approach, and the one we target here, is to use electrolytes that sparsely dissolve PS *e.g.* highly concentrated^[16] or fluorinated ether-based electrolytes.^[17–24]

Sulfur and PS solubility in fluorinated ethers are several orders of magnitude lower as compared to linear glymes.^[17,21,25] For instance, Azimi et al.^[20] showed, by *ex situ* high-performance liquid chromatography (HPLC) precipitation of PS in a fluorinated ether (1,1,2,2-tetrafluoroethyl-2,2,3,3-tetrafluoropropyl ether, TTE) based electrolyte, that the PS tend to accumulate inside the electrode, making migration to the anode less likely. Moreover, fluorinated ethers are capable of forming a stable SEI without additional additives. Gu et al.,^[16] studied the lithium stability in a 1,3-(1,1,2,2-tetrafluoroethoxy)propane (FDE) fluorinated ether-based electrolyte and revealed that the resulting SEI layer consists of insoluble lithium fluoride (LiF) and sulfate/sulfite/sulfide species which serve as a self-limiting layer, suppressing parasitic reactions on the lithium metal.

Dominko et al.,^[24] reported a comparative *in situ* characterization of sulfur reduction in different electrolytes using X-ray absorption spectroscopy stating that sulfur conversion process is not affected by the decreased PS solubility in fluorinated ethers and observed long and short PS at the cathode surface during cycling. No direct analysis, however, was performed with respect to selective PS solubility or diffusion.

Here, we have used operando confocal Raman spectroscopy to study the PS solubility and diffusion in electrolytes employing two different fluorinated ethers with different degrees of fluorination: (1,2-(1,1,2,2-tetrafluoroethoxy)ethane (TFEE) and 1,1,2,2-tetrafluoroethylmethyl ether (TFEME) (Fig-

[a] Dr. R. Bouchal,[†] Dr. A. Boulaoued,[†] Prof. P. Johansson

Department of Physics
Chalmers University of Technology
412 96 Gothenburg, Sweden
E-mail: patrik.johansson@chalmers.se

[b] Prof. P. Johansson
ALISTORE-ERI, CNRS FR 3104
Hub de l'Energie
80039 Amiens Cedex, France

[†] These authors contributed equally to this work.

Supporting information for this article is available on the WWW under
<https://doi.org/10.1002/batt.201900188>

An invited contribution to a Special Collection dedicated to the Symposium on Batteries and Supercapacitors at the E-MRS Spring Meeting 2019

© 2020 The Authors. Published by Wiley-VCH Verlag GmbH & Co. KGaA.
This is an open access article under the terms of the Creative Commons Attribution License, which permits use, distribution and reproduction in any medium, provided the original work is properly cited.

ure 1). We show that only short-chain PS are soluble and diffuse towards the anode.

To probe the PS solubility and diffusion, *operando* confocal Raman spectra were recorded from the anode side during cycling, using a special home-built cell.^[26,27] The laser spot was adjusted to probe a volume within the separator facing the anode. In that way, only PS which have diffused from the cathode to the anode are recorded. As this approach combined with the set-up is novel, and the resulting data rather difficult to analyze unambiguously, we start by using a conventional DME based electrolyte before moving on to the fluorinated ether-based electrolytes. To enable the best possible comparison with the fluorinated electrolytes, no LiNO₃ was added to the reference cell with the DME based electrolyte and thus this cell could not be completely charged (Figure S1).

The cell configuration was optimized by reducing the electrolyte to sulfur (E/S) ratio (17 µl/mg) and limiting the cycling rate (C/20) while ensuring that proper spectra were possible to record. This is far from easy, why many experiments reported in the literature have been conducted with much higher ratios and even slower rates.^[28–31] The cell set-up and confocal spot together with the charging/discharging conditions means that only the PS formed that are soluble and then have diffused to end up near the lithium anode are monitored, whereas the PS formed at the cathode side are not recorded.

The formation of PS during cycling in ether-based electrolytes has already been reported by several groups, both by Raman spectroscopy and other techniques.^[29,30,32–36] It is commonly accepted that the high voltage plateau at 2.4–2.3 V is related to the S₈ ring opening and long-chain PS Li₂S_n ($n=5–8$) formation, whereas short-chain PS Li₂S_n ($n=1–4$) are the main species involved in the second plateau at 2.1 V.^[36,37] Our results for a DME based electrolyte show similar behavior (Figures S1, S2); upon discharge, the voltage profile begins with a slope at 2.34 V, the absence of the first plateau being due to the high solubility of S₈ and its chemical reduction in the electrolyte. Long- and short-chain PS are involved during the slope (2.34–2.12 V). Our assignment of the PS species is based mainly on reports on PS in solution and various in situ characterization studies (Table S1). The peak with a high intensity at 397 cm⁻¹ is assigned to S₆²⁻^[26,29,38] and this corresponds well to the calculated value by Steudel et al.^[39] The peak at 502 cm⁻¹ can be attributed to long-chain PS, S_n²⁻ ($n=7$ or 8).^[40,41] Despite that no unambiguous/individual assignment of these PS species is established,^[42,43] our assignment is supported by the voltage curve as the peak at 502 cm⁻¹ shifts down to 484 cm⁻¹ during the slope (2.34–2.12 V) and this process also continues slightly during the first plateau,

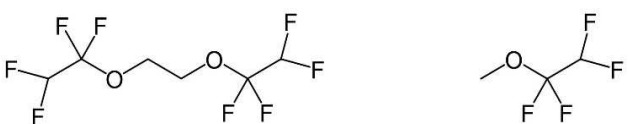


Figure 1. Chemical structures of the fluorinated ethers: left: 1,1,2,2-tetrafluoroethoxyethane (TFEE) and right: 1,1,2,2-tetrafluoroethylmethyl ether (TFEME).

indicating the reduction of long-chain PS (S_n²⁻, $n=7–8$) to short-chain PS. For the latter, the peak at 532 cm⁻¹ is well known to be related to the tri-sulfur radical S₃^{•-}^[26,29–32,44,45] and S₄²⁻ is observed at 448 cm⁻¹^[29,30,38,46–48] and possibly also contributes to the peak at 484 cm⁻¹ besides S_n²⁻ ($n=4–8$).^[29,30,32,41,49,50]

The evolution of the integrated areas of the main peaks (Figure S4) shows that S₆²⁻ decreases considerably at the beginning of the second plateau and vanishes completely at the end, while S₄²⁻ and S₃^{•-} disappear later. During the charging, S₃^{•-} reappears first, followed by S₆²⁻ and S₄²⁻ increasing gradually. Our results hence confirm the solubility and the diffusion of both long- and short-chain PS in DME based electrolytes.

The fluorinated ether-based electrolytes show a completely different behaviour as compared to the non-fluorinated. The two full discharge-charge cycles (Figure 2, S6) do not present any shuttle effect and demonstrate a systematic appearance and disappearance of PS. During the first discharge (D₁), only peaks related to the electrolyte (Figure S2) can be observed. Starting from the first slope, three main peaks appear at 406, 452 cm⁻¹ and 494 cm⁻¹ which are assigned to S₄²⁻.^[29,30,32,46–48,51] These assignments are based on reports for PS in solution, but also if we compare to S₄²⁻ and S₅²⁻ in the solid state, they appear at approximately the same wavenumbers (Table S1). Moreover, two reports^[48,51] have shown the ambiguity in making individual assignment of S₅²⁻ in solution, why a contribution from S₅²⁻ cannot be completely ruled out, but nevertheless, we can confirm the absence of long-chain PS. At the centre of the second plateau, S₄²⁻ vanishes completely which is consistent with a liquid-solid conversion from Li₂S₄ to Li₂S₂ and Li₂S. When the cell is charged (C₁), the three peaks re-appear in the second plateau at ca. 2.32 V with an additional very weak peak at ca. 235 cm⁻¹, attributed to S₄²⁻ bending.^[31,32] The second cycle (D₂ + C₂) demonstrates the exact same behaviour and hence good reproducibility and stability.

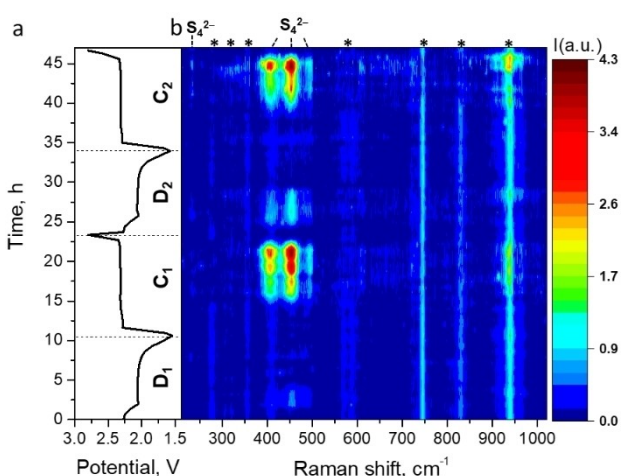


Figure 2. Operando Raman spectroscopy of a Li–S battery: a. Potential profile of the C/S composite cathode using a 1 M LiTFSI in TFEE:DOL electrolyte at C/20 rate with a 17 µl/mg E/S ratio, and b. A heatmap representation of the evolution of the Raman spectra using a 676 nm laser excitation wavelength. * = electrolyte peaks (Figure S5).

These results are also confirmed by additional experiments carried out before optimizing the E/S ratio and C-rate (Figure S7) wherein S_4^{2-} features again are found at 250, 405, 452 and 493 cm^{-1} and with an additional peak at 199 cm^{-1} which as well can be assigned to S_4^{2-} .^[30,32,41,46–48,51]

The DOL band at *ca.* 940 cm^{-1} , due to C–O and C–C stretching vibrations,^[52] broadens during the formation of short-chain PS. This hints to PS solvation by DOL rather than TFEE, in agreement with reports showing that the solubility of both LiTFSI and PS in TFEE is very low.^[17,53] This is further strengthened by the S_4^{2-} peak being at 452 cm^{-1} in TFEE, slightly up-shifted *vs.* in DME, following the behaviour of TFSI: the peak at 745 cm^{-1} in TFEE is at 740 cm^{-1} in DME. This might indicate that the cation-anion interactions for both Li_2S_4 and LiTFSI are stronger in TFEE.^[54]

To correlate the electrochemistry with the PS formation, the evolution of the Raman peak areas as a function of cycling time was studied together with the cell potential (Figure 3). The amount of PS that has diffused to the probed volume as a function of time can be determined by the peak areas. During D_1 (Figure 2), the peak areas corresponding to S_4^{2-} develop in the middle of the first slope until they all reach a maximum at the beginning of the second plateau, where they shortly afterwards decrease and vanish completely in the middle of the plateau – corresponding to *ca.* 5 h discharge. During C_1 and at the starting of the second plateau, S_4^{2-} appears but in much higher amounts than observed in D_1 . The second cycle shows quite similar behaviour – testifying the good reversibility and stability of the system. The differences seen in the peak areas during discharge, i.e. larger and with a slightly earlier appearance in D_2 , could be explained by S_4^{2-} needing more time to migrate out from the cathode to the anode side in D_1 . By comparing the formation of S_4^{2-} with respect to the electrochemical process, the S_4^{2-} observed at the anode side is completely in line with results previously reported for tetraglyme (TEGDME) and DME based electrolytes,^[24,26,30,32,33] showing that S_4^{2-} is mainly formed at the first voltage slope in the discharge, and is gradually reduced to S_2^{2-} or S_2^- during the

second plateau. Upon charge, S_4^{2-} appears again between the first and the second plateau at potentials *ca.* 2.3 V.

The second electrolyte studied, based on the fluorinated ether TFEME (Figures 4, S8), provides essentially the same results as for TFEE; S_4^{2-} can be found at 410 and $\sim 452\text{--}456\text{ cm}^{-1}$ and 490 cm^{-1} , but the peaks are unfortunately not as well defined as in the TFEE spectra, which makes it hard to unambiguously track the peak maxima and positions. Overall, there are no long-chain PS detected and the observed S_4^{2-} corresponds to the electrochemical formation potential. As an example, the peak area of the band at 455 cm^{-1} (Figure S10) reaches a maximum at the second plateau in D_1 at *ca.* 2.1 V and disappears at the end of discharge. Upon charge (C_1), it shows up again at a maximum corresponding to the beginning of the second plateau and vanishes at the end of charge. However, the latter behaviour was not reversible in the second cycle ($D_2 + C_2$).

By operando confocal Raman spectroscopy, we can directly provide evidence of selective solubility and diffusion across the separator of PS in fluorinated ether-based electrolytes. Long-chain PS S_n^{2-} ($n=5\text{--}8$) are not soluble, in contrast to S_4^{2-} detected in the electrolyte at the anode side. This selective feature makes using fluorinated ethers a very promising route to reduce the shuttling problem in Li–S battery electrolytes. Tailoring new fluorinated ether-based electrolytes to achieve the best cycling performance possible relies on a further understanding of the interactions between PS and electrolyte components, as well as establishing the corresponding PS redox processes. This could be obtained by coupling other techniques (EPR, UV, IR or XAS) with Raman spectroscopy, to ascertain, at every electrochemical cycling step, the same distribution of PS species formed.

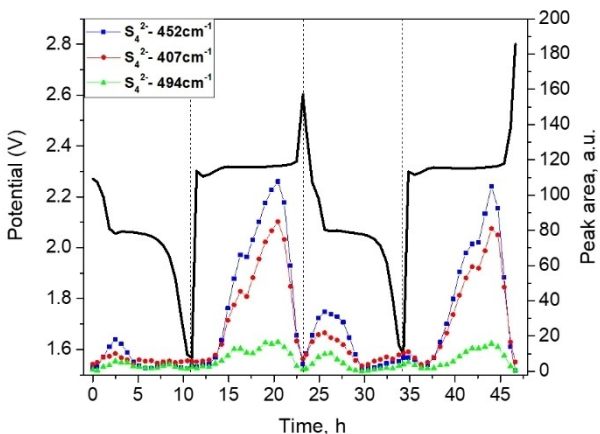


Figure 3. The peak areas of Raman features corresponding to different PS species upon cycling in the 1 M LiTFSI in TFEE:DOL electrolyte. The intensities are normalized to the TFSI peak intensity at *ca.* 740 cm^{-1} .

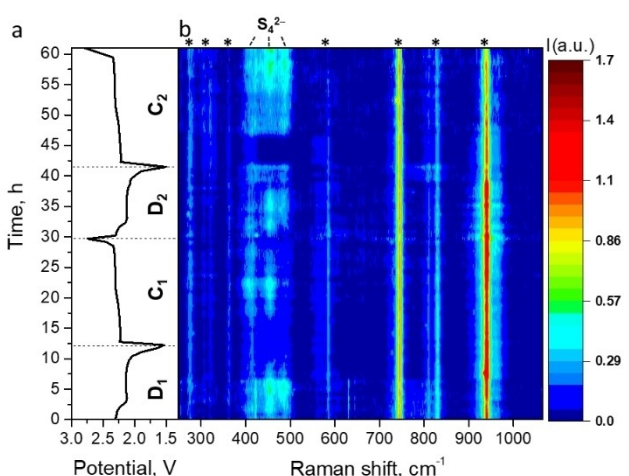


Figure 4. Operando Raman spectroscopy of a Li–S battery cell: **a**, Potential profile of the C/S composite cathode using a 1 M LiTFSI in TFEME:DOL electrolyte at C/20 rate with an $18\text{ }\mu\text{l/mg}$ E/S ratio, and **b**, a heatmap representation of the evolution of the Raman spectra using a 676 nm laser excitation wavelength. * = electrolyte (Figure S9).

Experimental Section

Experimental Details.

Chemicals: Lithium bis(trifluoromethanesulfonyl)imide (LiTFSI, 99.95%) was purchased from Solvionic. 1,3-dioxolane (DOL) (anhydrous, 99.8% with 75 ppm butylated hydroxytoluene as inhibitor) and dimethylether (DME) were obtained from Sigma-Aldrich. 1,2-(1,1,2,2-tetrafluoroethoxy)ethane (TFEE) and 1,1,2,2-tetrafluoroethylmethyl ether (TFEME, 98%) were bought from Apollo Scientific. The C/S composite electrodes were provided from the ISIT Fraunhofer institute and had a 60% S loading. Whatman glass fibre (GF/D, 675 µm) was used as a separator.

Drying: LiTFSI was dried overnight at 120°C under vacuum in a Bucchi oven. All the solvents were dried before use. The solvents were in contact with already activated molecular sieves. After two days, the solvents were filtered out by using a 450 nm PTFE filter to remove any dust resulted from the sieves. The water content was checked by using Karl-Fischer titration and was found to be <8 ppm. The C/S composite cathodes were dried at 45°C under vacuum overnight.

Cell assembly and analysis: 16 mmØ C/S composite electrodes were used as cathodes and 18 mm Ø lithium discs as counter electrodes. The lithium foil was brushed to remove any surface layer and then pressed to obtain a homogeneous and smooth surface. Afterwards, a 2 mm Ø hole was made in the lithium disc. One Whatman separator was used together with ca. 100 µl of electrolyte corresponding to 16–18 µl/mg electrolyte to sulfur (E/S) ratio. Three different electrolytes were used: 1 M LiTFSI in a mixture of ether (TFEE, TFEME or DME) and dioxolane 1:1 by volume. The assembly of the cells was done in an argon-filled glove box with an O₂ and H₂O content below 1 ppm.

The galvanostatic cycling tests were performed with a Gamry Series G 300 galvanostat. at room temperature between 1.5 and 2.8 V versus Li⁺/Li⁺ at C/20 rate (C/n = 1 Li/n h).

Operando Raman spectroscopy: The Raman spectra were collected at room temperature using a nitrogen-cooled CCD detector connected to a Dilor XY 800 spectrometer (Horiba GmbH), equipped with a 676 nm Ar/Kr laser operated at a power <4 mW on the sample surface, an 1800 grooves/mm grating, a 300 mm focal length and a pinhole size of 400 µm. The spectra were collected in backscattering geometry with a 10X objective (confocal micro-Raman mode). To increase the signal-to-noise ratio (S/N), each spectrum is the average of 10 accumulations of 2 min each at a resolution of approximately 2 cm⁻¹. The focal plane was adjusted to be at the separator surface and very close to the edge of the hole in the Li anode, in order to reduce the effect of inhomogeneity of the electric field line distribution. Spectral processing consisted essentially of removing spikes and background correction. The spectra shown in the operando experiments have been normalized to the TFSI peak intensity at ca. 740 cm⁻¹.

Acknowledgements

The European Commission has provided financial support for "High-Energy Lithium Sulfur Cells and Batteries" (HELIS) under research grant agreement No. 666221.

Keywords: fluorinated ethers · polysulfides · diffusion · Li–S batteries · operando Raman spectroscopy

- [1] M. Li, J. Lu, Z. Chen, K. Amine, *Adv. Mater.* **2018**, *30*, 1800561.
- [2] G. Zubi, R. Dufo-López, M. Carvalho, G. Pasaoglu, *Renewable Sustainable Energy Rev.* **2018**, *89*, 292–308.
- [3] B. Dunn, H. Kamath, J. Tarascon, *Science* **2011**, *334*, 928–936.
- [4] G. Zubi, R. Dufo-López, M. Carvalho, G. Pasaoglu, *Renewable Sustainable Energy Rev.* **2018**, *89*, 292–308.
- [5] S. H. Chung, A. Manthiram, *Adv. Mater.* **2019**, *31*, 1901125.
- [6] R. Fang, S. Zhao, Z. Sun, D.-W. Wang, H.-M. Cheng, F. Li, *Adv. Mater.* **2017**, *29*, 1606823.
- [7] T. Cleaver, P. Kovacik, M. Marinescu, T. Zhang, G. Offer, *J. Electrochem. Soc.* **2018**, *165*, A6029–A6033.
- [8] J. Scheers, S. Fantini, P. Johansson, *J. Power Sources* **2014**, *255*, 204–218.
- [9] Q. Pang, X. Liang, C. Y. Kwok, L. F. Nazar, *Nat. Energy* **2016**, *1*, 1–11.
- [10] P. Bonnick, E. Nagai, J. Muldoon, *J. Electrochem. Soc.* **2018**, *165*, A6005–A6007.
- [11] S. S. Zhang, *J. Power Sources* **2016**, *322*, 99–105.
- [12] L. Zhang, M. Ling, J. Feng, L. Mai, G. Liu, J. Guo, *Energy Storage Mater.* **2018**, *11*, 24–29.
- [13] A. Gupta, A. Bhargav, A. Manthiram, *Adv. Energy Mater.* **2019**, *9*, 1–9.
- [14] X. Yu, A. Manthiram, *Acc. Chem. Res.* **2017**, *50*, 2653–2660.
- [15] H. Shi, W. Lv, C. Zhang, D.-W. Wang, G. Ling, Y. He, F. Kang, Q.-H. Yang, *Adv. Funct. Mater.* **2018**, *28*, 1800508.
- [16] S. Gu, R. Qian, J. Jin, Q. Wang, J. Guo, S. Zhang, S. Zhuo, Z. Wen, *Phys. Chem. Chem. Phys.* **2016**, *18*, 29293–29299.
- [17] S. Drvarič Talian, S. Jeschke, A. Vizintin, K. Pirnat, I. Arčon, G. Aquilanti, P. Johansson, R. Dominko, *Chem. Mater.* **2017**, *29*, 10037–10044.
- [18] H. Lu, Y. Yuan, Z. Hou, Y. Lai, K. Zhang, Y. Liu, *RSC Adv.* **2016**, *6*, 18186–18190.
- [19] N. Azimi, W. Weng, C. Takoudis, Z. Zhang, *Electrochem. Commun.* **2013**, *37*, 96–99.
- [20] N. Azimi, Z. Xue, I. Bloom, M. L. Gordin, D. Wang, T. Daniel, C. Takoudis, Z. Zhang, *ACS Appl. Mater. Interfaces* **2015**, *7*, 9169–9177.
- [21] C. Zu, N. Azimi, Z. Zhang, A. Manthiram, *J. Mater. Chem. A* **2015**, *3*, 14864–14870.
- [22] M. Gao, C. Su, M. He, T. Glossmann, A. Hintennach, Z. Feng, Y. Huang, Z. Zhang, *J. Mater. Chem. A* **2017**, *5*, 6725–6733.
- [23] H. Lu, Y. Yuan, K. Zhang, F. Qin, Y. Lai, Y. Liu, *J. Electrochem. Soc.* **2015**, *162*, A1460–A1465.
- [24] R. Dominko, A. Vizintin, G. Aquilanti, L. Stievano, M. J. Helen, A. R. Munnangi, M. Fichtner, I. Arcon, *J. Electrochem. Soc.* **2018**, *165*, A5014–A5019.
- [25] M. L. Gordin, F. Dai, S. Chen, T. Xu, J. Song, D. Tang, N. Azimi, Z. Zhang, D. Wang, *ACS Appl. Mater. Interfaces* **2014**, *6*, 8006–8010.
- [26] J. Hannauer, J. Scheers, J. Fullenwarth, B. Fraisse, L. Stievano, P. Johansson, *ChemPhysChem* **2015**, *16*, 2755–2759.
- [27] G. Fredi, S. Jeschke, A. Boulouqued, J. Wallenstein, M. Rashidi, F. Liu, R. Harnden, D. Zenkert, J. Hagberg, G. Lindbergh, *Multifunct. Mater.* **2018**, *1*, 015003.
- [28] J. D. McBrayer, T. E. Beechem, B. R. Perdue, C. A. Apblett, F. H. Garzon, *J. Electrochem. Soc.* **2018**, *165*, A876–A881.
- [29] M. Hagen, P. Schiessl, M. Hammer, S. Dorfler, J. Tubke, M. J. Hoffmann, H. Althues, S. Kaskel, *J. Electrochem. Soc.* **2013**, *160*, A1205–A1214.
- [30] W. Zhu, A. Paoella, C. S. Kim, D. Liu, Z. Feng, C. Gagnon, J. Trottier, A. Vijn, A. Guerfi, A. Mauger, *Sustain. Energy Fuels* **2017**, *1*, 737–747.
- [31] H. L. Wu, L. A. Huff, A. A. Gewirth, *ACS Appl. Mater. Interfaces* **2015**, *7*, 1709–1719.
- [32] J. J. Chen, R. M. Yuan, J. M. Feng, Q. Zhang, J. X. Huang, G. Fu, M. Sen Zheng, B. Ren, Q. F. Dong, *Chem. Mater.* **2015**, *27*, 2048–2055.
- [33] M. Cuisinier, P. E. Cabelguen, S. Evers, G. He, M. Kolbeck, A. Garsuch, T. Bolin, M. Balasubramanian, L. F. Nazar, *J. Phys. Chem. Lett.* **2013**, *4*, 3227–3232.
- [34] Y. Gorlin, M. U. M. Patel, A. Freiberg, Q. He, M. Piana, M. Tromp, H. A. Gasteiger, *J. Electrochem. Soc.* **2016**, *163*, A930–A939.
- [35] Q. Zou, Y. C. Lu, *J. Phys. Chem. Lett.* **2016**, *7*, 1518–1525.
- [36] L. Zhang, T. Qian, X. Zhu, Z. Hu, M. Wang, L. Zhang, T. Jiang, J. H. Tian, C. Yan, *Chem. Soc. Rev.* **2019**, *48*, 5432–5453.
- [37] M. Wild, L. O'Neill, T. Zhang, R. Purkayastha, G. Minton, M. Marinescu, G. J. Offer, *Energy Environ. Sci.* **2015**, *8*, 3477–3494.
- [38] J.-J. Chen, R.-M. Yuan, J.-M. Feng, Q. Zhang, J.-X. Huang, G. Fu, M.-S. Zheng, B. Ren, Q.-F. Dong, *Chem. Mater.* **2015**, *27*, 2048–2055.

- [39] R. Steudel, Y. Steudel, *Chem. Eur. J.* **2013**, *19*, 3162–3176.
- [40] T. Chivers, F. Edelmann, J. F. Richardson, K. J. Schmidt, *Can. J. Chem.* **1986**, *64*, 1509–1513.
- [41] R. Steudel, F. Schuster, *Z. Naturforsch. A* **1977**, *32*, 1313–1319.
- [42] M. K. Richard, C. Alkire, P. N. Bartlett Eds., *Electrochemical Engineering: The Path from Discovery to Product*, Wiley **2018**.
- [43] R. Steudel, T. Chivers, *Chem. Soc. Rev.* **2019**, *48*.
- [44] T. Chivers, P. J. W. Elder, *Chem. Soc. Rev.* **2013**, *42*, 5996.
- [45] T. Chivers, I. Drummond, *Inorg. Chem.* **1972**, *11*, 2525–2527.
- [46] A. T. Ward, *Mater. Res. Bull.* **1969**, *4*, 581–590.
- [47] G. J. Janz, J. R. Downey, E. Roduner, G. J. Wasilczyk, J. W. Coutts, A. Eluard, *Inorg. Chem.* **1976**, *15*, 1759–1763.
- [48] H. Hermann, G. Wieghardt, H. Kleinschmager, G. Weddigen, *Z. Naturforsch.* **1976**, *31*, 415–418.
- [49] O. El Jaroudi, E. Picquenard, A. Demortier, J. P. Lelieur, J. Corset, *Inorg. Chem.* **2000**, *39*, 2593–2603.
- [50] R. Steudel, T. Chivers, *Chem. Soc. Rev.* **2019**, *48*, 3279–3319.
- [51] P. Dubois, J. P. Lelieur, G. Lepoutre, *Inorg. Chem.* **1988**, *27*, 73–80.
- [52] V. Mohaček-Grošev, K. Furić, H. Ivanković, *Vib. Spectrosc.* **2013**, *64*, 101–107.
- [53] S. Jeschke, P. Johansson, *Chem. Eur. J.* **2017**, *23*, 9130–9136.
- [54] J. Wang, Y. Yamada, K. Sodeyama, C. H. Chiang, Y. Tateyama, A. Yamada, *Nat. Commun.* **2016**, *7*, 1–9.

Manuscript received: November 22, 2019
Revised manuscript received: January 22, 2020
Accepted manuscript online: January 22, 2020
Version of record online: January 29, 2020